



SLOVAK UNIVERSITY OF TECHNOLOGY IN BRATISLAVA
FACULTY OF ELECTRICAL ENGINEERING AND INFORMATION TECHNOLOGY

Ing. Ivana Klačková
Dissertation Thesis Abstract

Radiation Damage Studies of the ePix100 Detector at the EuXFEL

to obtain the Academic Title of philosophiae doctor

In the doctorate degree study programme: Physical Engineering
In the field of study: Electrical and Electronics Engineering
Form of study: Full-time

June 2021

The dissertation thesis has been prepared at the Institute of Nuclear and Physical Engineering, FEEIT SUT in Bratislava and at the European X-Ray Free Electron Laser GmbH.

Submitter: **Ing. Ivana Klačková**
Slovak University of Technology in Bratislava,
Faculty of Electrical Engineering and Information Technology,
Institute of Nuclear and Physical Engineering,
Ilkovičova 3, 812 19 Bratislava, Slovakia,
European XFEL GmbH,
Holzkoppel 4, 22869 Schenefeld, Germany

Supervisors: **doc. Ing. Andrea Šagátová, PhD.**
Slovak University of Technology in Bratislava,
Faculty of Electrical Engineering and Information Technology,
Institute of Nuclear and Physical Engineering,
Ilkovičova 3, 812 19 Bratislava

Dr. Markus Kuster
European XFEL GmbH,
Holzkoppel 4, 22869 Schenefeld, Germany

Dr. Steffen Hauf
European XFEL GmbH,
Holzkoppel 4, 22869 Schenefeld, Germany

Opponents: **Prof. RNDr. Branislav Sitár, DrSc.**
Comenius University in Bratislava,
Faculty of Mathematics, Physics and Informatics,
Department of Nuclear Physics and Biophysics,
Mlynská dolina F1, 842 48 Bratislava

Dr. Bernd Schmitt
Paul Scherrer Institute,
Forschungsstrasse 111, 5232 Villigen PSI, Switzerland

The dissertation thesis abstract was submitted on: the 9th of June 2021

The dissertation thesis defence will be held on:

at.....h, **online**

prof. Dr. Ing. Miloš Oravec
Dean of FEI STU

Abstrakt

European XFEL (X-ray Free Electron Laser), európsky röntgenový laser voľných elektrónov (ďalej len röntgenový laser), je v súčasnosti najväčší zdroj röntgenového laserového žiarenia na svete, ktorý sa vyznačuje vysokou brilanciou a ultra-krátkymi pulzami s vysokou opakovacou frekvenciou. Prevádzkovanie detektora v jeho radiačnom poli predstavuje pre detektor a jeho komponenty vysoké riziko radiačného poškodenia. Štúdium poškodenia indukovaného žiarením je nevyhnutné pre pochopenie jeho vplyvu na kvalitu meraní realizovaných detektorom, a tiež na odhad životnosti takéhoto detektora. Cieľom práce bolo vyhodnotenie účinkov radiačného poškodenia na detektor ePix100a. Ide o detektor, ktorý je súčasťou ePix platformy zastrešujúcej rôzne typy hybridných pixelových detektorov vyvíjaných pre použitie na röntgenových laserových zariadeniach. V European XFEL sa používa na dvoch experimentálnych stanicích. Detektor ePix100a bol ožarovaný priamym a čiastočne odtieneným röntgenovým laserovým zväzkom za kontrolovaných podmienok. Účelom bolo systematické štúdium vplyvu radiáciou indukovaného poškodenia na operačné parametre detektora. V štúdiu sme sledovali a vyhodnocovali parametre, ktoré sú podstatné pre zabezpečenie správneho fungovania detektora počas vedeckých experimentov, ako napríklad offset, šum, konverzný faktor, alebo energetické rozlíšenie. Pri experimente sme pozorovali radiačné poškodenie nielen senzora, ale aj vyčítavacej elektroniky. V polovodičovom senzore detektora sa radiačné poškodenie prejavilo najmä nárastom zvodového prúdu. V prípade vyčítavacej elektroniky sa poškodenie prejavilo ako zmena v konverznom faktore. Získané výsledky sa použili na odhad životnosti detektora pri jeho dlhodobom používaní. Výrazné zníženie dynamického rozsahu ($R_{DR} > 50\%$) sa očakáva pre absorbovanú dávku $> 7.4 \text{ MGy}$ pre integračný čas $t_{\text{Int}} = 50 \mu\text{s}$ na rozhraní Si-SiO₂ a pre $t_{\text{Int}} = 800 \mu\text{s}$ je hraničná dávka 131 kGy. Z týchto odhadov je zrejmé, že ePix100a môže byť používaný niekoľko rokov bez výrazného zhoršenia parametrov za predpokladu, že intenzita röntgenového laserového zväzku pri experimentoch nepresiahne dynamický rozsah detektora o niekoľko rádov. Získané výsledky poskytujú cenné informácie pre používanie detektora ePix100a na podobných röntgenových laserových zariadeniach. Pozorovania a závery plynúce z tejto práce sú tiež relevantné pre budúci vývoj radiačne odolnejšieho detektora pre danú aplikáciu.

Kľúčové slová: detektory RTG žiarenia, radiačné poškodenie polovodičových detektorov, charakterizácia detektora, röntgenový laser voľných elektrónov

Abstract

The European X-ray Free Electron Laser (EuXFEL) is the world's fastest and most brilliant X-ray laser source, characterized by high brilliance, high repetition rate and ultra-short X-ray pulses. Detector operation in its radiation environment poses a high risk of radiation damage to a detector and its components. Knowledge about radiation-induced damage is vital for understanding its influence on the quality of scientific data and a detector's lifetime. This thesis aims to evaluate the effects of radiation-induced damage on the ePix100a detector. The ePix100a is a member of the ePix detector family, which is used to support various applications at FEL facilities world wide. At the European XFEL, it is used at two scientific instruments: the High Energy Density (HED) instrument and the Material Imaging and Dynamics (MID) instrument. The ePix100a detector was irradiated under controlled conditions with a direct, attenuated FEL beam to systematically study the effects of the induced radiation damage on various detector parameters that are commonly used as indicators of the good scientific performance of a detector, i.e., offset, noise, gain, and energy resolution. During the radiation damage study of the ePix100a, we have observed damage in the sensor and the Application Specific Integrated Circuit (ASIC). The observed radiation-induced damage effects in the sensor were mainly due to an increase in the leakage current. We have observed changes in the detector gain on ASIC level due to damage induced in the pixels' readout electronics. Based on the obtained results, the limits for the long-term operation of the ePix100a at EuXFEL and other light sources in consideration of its scientific performance have been assessed. Significant reduction of the dynamic range, i.e. $R_{\text{DR}} > 50\%$ for $t_{\text{Int}} = 50 \mu\text{s}$ is expected with a dose absorbed in the Si-SiO₂ interface $> 7.4 \text{ MGy}$ and for $t_{\text{Int}} = 800 \mu\text{s}$ at 131 kGy . We have determined that the ePix100a can be used without significant degradation of its operating performance for several years if the incident photon beam intensities do not outperform the detector's dynamic range by several orders of magnitude. The results we have obtained provide valuable input for the ePix100a operation at FEL facilities. The observations and conclusions made are also relevant for future optimization towards radiation-harder detectors for photon science.

Key words: X-ray detectors, Radiation damage of semiconductor detectors, Detector performance characterization, Free-electron laser

Contents

| | | |
|----------|---|-----------|
| 1 | Introduction | 5 |
| 2 | State of the Art | 6 |
| 2.1 | X-ray Radiation Damage in MOS Devices | 8 |
| 2.2 | Effects of Radiation-Induced Damage on MOS Devices | 9 |
| 2.2.1 | Threshold Voltage Change | 9 |
| 2.2.2 | Increase of Leakage Current | 9 |
| 2.2.3 | Decrease of Charge Transfer Efficiency | 11 |
| 2.2.4 | Decrease of Breakdown Voltage | 11 |
| 2.2.5 | Decrease of Charge Carrier Mobility | 11 |
| 2.3 | Detector Performance Parameters Relevant for Radiation Damage | 12 |
| 2.3.1 | Dark Signal | 12 |
| 2.3.2 | Dynamic Range | 13 |
| 2.3.3 | Energy Resolution | 14 |
| 2.3.4 | Signal-To-Noise Separation | 15 |
| 2.3.5 | Absolute Gain | 15 |
| 3 | Dissertation Thesis Aims | 15 |
| 4 | Experiment Methodology | 16 |
| 4.1 | The ePix100a Detector | 16 |
| 4.2 | Experiment Setup and Methods | 17 |
| 4.2.1 | Dose Evaluation | 19 |
| 5 | Results | 20 |
| 5.1 | Immediate Effects | 20 |
| 5.2 | Post-Irradiation Performance | 22 |
| 5.2.1 | Offset and Noise | 22 |
| 5.2.2 | Gain and Energy Resolution | 25 |
| 5.3 | Lifetime Estimates | 27 |
| 6 | Main Findings and Contributions of the Thesis | 30 |
| 7 | Conclusions and Outlook | 31 |
| 8 | Zhrnutie | 33 |
| | References | 35 |
| | List of Author's Publications | 40 |

1 Introduction

The European XFEL, an international research facility located in the metropolitan area of Hamburg, Germany, started user operation in September 2017. As the world's most brilliant X-ray source, it enables scientific research using ultrafast spatially coherent pulses. The EuXFEL provides the highest brilliance amongst FEL sources and exceeds common synchrotrons by nine orders of magnitude [1].

The EuXFEL's linear accelerator delivers electron bunches with energies of up to 17.5 GeV. The highly energetic electrons undergo a Self Amplified Spontaneous Emission (SASE) process by which, each second 27 000 pulses, each containing up to 10^{12} photons, are produced. X-ray pulses with an energy between 0.25 keV and 25 keV are delivered on a time duration as short as units of femtoseconds, with a pulse energy amounting to more than 10 mJ [1]. The linear accelerator (LINAC) that is used to bring electrons up to an energy of 17.5 GeV can drive several undulator systems at the same time. Each undulator system constitutes a SASE beamline. For each beamline, X-ray radiation with different properties can be generated for the different, simultaneously operating experiment end-stations. At the European XFEL, three SASE beamlines are operated: SASE 1, SASE 2 and SASE 3. Each beamline serves two scientific instruments, thus six different experimental stations are available to users in total. The scientific instruments are discussed in greater detail by Tschentscher et al. [1].

The ePix100a detector [2] is a hybrid pixel detector designed for low noise spectroscopy applications and is a member of the ePix detector family providing hybrid pixel detectors to support a wide range of applications at FEL facilities. At the European XFEL the ePix100a is used at two scientific instruments, namely High Energy Density (HED) [3] and Material Imaging and Dynamics (MID) [4]. The ePix100a plays a key role in the experimental program of the HED instrument. Hence its good scientific performance is essential. The detector is required to provide low noise, i.e. $< 80 e^-$ RMS (root-mean-square) and a photon peak-to-noise separation $\geq 5 \sigma$ @ 5 keV, thus an radiation-induced noise increase is an important parameter to observe and evaluate closely. Another important parameter is the detector's dynamic range, as its significant reduction will lead to a decreased capability to resolve high-intensity signals.

Understanding the effects of radiation-induced damage on the detector's performance and assessing the detector's lifetime is essential to ensure reliable scientific operation. It is important to provide a time frame for damage compensation measures to take place in terms of re-calibration, repair or module exchange. The thesis aimed to investigate the radiation damage of the ePix100a since its tolerance to FEL radiation has not been assessed before through a dedicated study in a controlled environment.

2 State of the Art

The unique properties of the EuXFEL beam and each beamline's experiments set demanding requirements towards detector performance and capabilities [5, 6]. As there was no existing detector technology capable of satisfying the requirements resulting from the EuXFEL time structure (4.5 MHz frame rate), intensity of the FEL beam ($\approx 10^{12}$ photons/pulse) and specific needs of scientific instruments (e.g. single-photon sensitivity), a demand for novel detector systems arose. Each detector system was optimized to fulfil that portion of these requirements most important for the dedicated use-case of the experiment.

Several detectors were explicitly developed for the needs of the European XFEL, i.e. the Adaptive Gain Integrating Pixel Detector (AGIPD), the DEPFET Sensor with Signal Compression (DSSC) and the Large Pixel Detector (LPD). Other detector technologies primarily developed for other FEL facilities were adapted for such use at the EuXFEL. A summary of 2D detectors in use at the European XFEL is listed in Table 1, providing also reference for each detector.

Since high radiation tolerance is one of the requirements for these detectors, the AGIPD detector, together with the LPD detector, have been optimized to incorporate a higher level of radiation hardness into their design. Thorough studies of the influence of X-ray radiation on silicon sensors have been conducted during the design and development phase of the first generation of these detectors.

At the time of the AGIPD development, no previous studies were addressing highly irradiated silicon sensors by X-rays of the EuXFEL energies. Results by Zhang et al. [7, 8, 9] give insight on the parameters determining the damage depending on the induced dose and their influence on the operation of various types of silicon sensor designs. These studies provided valuable knowledge to design and optimize the sensor parameters as reported by Schwandt et al. [10, 11]. An overview of the AGIPD design challenges and development strategy is given by Klanner et al.[12].

The radiation hardness studies performed for the LPD detector [13] aimed to investigate X-ray radiation damage on different components of the detector assembly, e.g. sensor, ASIC, ASIC memory or bias circuitry. The observations led to an optimization of the assembly layers and to the addition of extra shielding for the most sensitive parts of the detector assembly, e.g. ASIC memory.

Other detectors, not explicitly built for but used at the EuXFEL, were also examined for their radiation hardness and exhibit a certain level of radiation tolerance, e.g. the JUNGFRÄU [14] detector.

The studies cited above provide helpful knowledge and valuable observations for the here presented study.

Table 1: Performance parameters of the 2D imaging pixel detectors in use at the European XFEL.

| 2D Detector | Pixel Size (μm^2) | | Energy Range (keV) | | Dynamic Range | | | EuXFEL Frame Rate | Maximum Frame Rate | Instrument |
|--------------------|-----------------------------------|---------------|-----------------------|------|--------------------|---|---------|----------------------|-----------------------|------------|
| AGIPD [15] | 200 | \times 200 | 3 | – 16 | 10^4 ph | @ | 12 keV | 4.5 MHz | 4.5 MHz | SPB, MID |
| DSSC DEPFET [16] | 204 | \times 236* | 0.5 | – 6 | 6×10^3 ph | @ | 1 keV | 4.5 MHz | 4.5 MHz | SCS, SQS |
| DSSC mini-SDD [17] | 204 | \times 236* | 0.5 | – 6 | 10^2 ph | @ | 1 keV | 4.5 MHz | 4.5 MHz | SCS, SQS |
| ePix100a [18, 19] | 50 | \times 50 | 2 | – 18 | 10^2 ph | @ | 8 keV | 10 Hz | 240 Hz | HED, MID |
| FastCCD [20, 21] | 30 | \times 30 | 0.25 | – 6 | 10^3 ph | @ | 0.5 keV | 10 Hz | 120 Hz | SCS |
| JUNGFRAU [22] | 75 | \times 75 | 3 | – 25 | 10^4 ph | @ | 12 keV | 10 Hz | 1.1 kHz | HED |
| LPD [23] | 500 | \times 500 | 5 | – 20 | 10^5 ph | @ | 12 keV | 4.5 MHz | 4.5 MHz | FXE |
| pnCCD [24] | 75 | \times 75 | 0.03 | – 25 | 6×10^3 ph | @ | 1 keV | 10 Hz | 150 Hz | SCS, SQS |

* Hexagonal pixels.

2.1 X-ray Radiation Damage in MOS Devices

The detectors' performance in a harsh radiation environment degrades due to the absorbed radiation dose inducing and triggering changes in the detector material. The basics principles of radiation-induced damage will be introduced in this chapter to understand the effects leading to radiation damage and degradation of detectors performance.

Radiation damage effects can be divided into two classes: bulk damage and surface damage. Bulk damage is caused by the interaction of an incident particle with the nuclei of the lattice atoms, causing their displacement from their lattice location [25, 26]. The displacement results in the creation of a Frenkel pair, silicon interstitial and a left-over vacancy. To displace a silicon atom from its lattice position, a minimum recoil energy E_d of approximately 25 eV [27] has to be imparted. Photons need an energy of at least 300 keV [28] in order to provide sufficient energy to create a Frenkel pair. This energy threshold is much higher than the energy provided by the EuXFEL beam. For photon energies < 300 keV, surface driven effects are expected, i.e. damage mainly at the Si-SiO₂ interface. Hence for the EuXFEL energy range (0.25 keV – 25 keV) only surface damage needs to be considered. In the following, only these relevant surface damage mechanisms are discussed in detail.

Surface damage originates in ionization energy losses of X-ray photons or charged particles and subsequently leads to an accumulation of space charges in or close to an insulating layer covering silicon (commonly SiO₂) and interfaces between this insulating layer and silicon. The density of the created charge is proportional to the amount of the radiation absorbed at or close to the interface. Mechanisms leading to surface damage are described in detail in various publications, to which the reader is referred [29, 30, 31]. These mechanisms can be divided into four steps:

- Generation of electron-hole pairs; the incoming radiation creates electron-hole pairs in the SiO₂. A fraction of electrons and holes recombine (depending on the type of radiation and the strength of electric field in the SiO₂). The effect of recombination for various incident particles is shown in Figure 1, where the fraction of unrecombined holes is shown as a function of the applied electric field.
- Transport of holes escaping recombination to the Si-SiO₂ interface; the electrons and holes escaping the recombination either, in case of electrons, drift towards the gate electrodes, or in case of the holes, transported to the Si-SiO₂ interface through a so called hopping via localized states present in the SiO₂.
- Formation of oxide charges; holes close to the Si-SiO₂ interface are captured by oxygen vacancies, thus forming positive charge in the oxide,

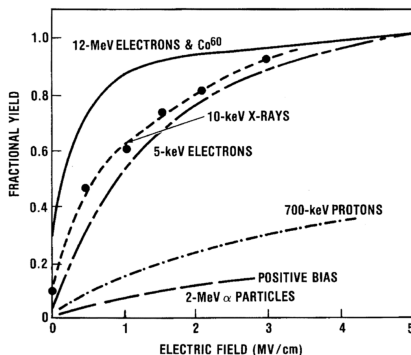


Figure 1: The fraction of holes escaping the initial recombination as a function of the applied field for different incident particle species. Figure adopted from [31].

known as oxide charge.

- Formation of interface traps; some of the holes during the transport react with hydrogenated oxygen vacancies and liberate protons. These protons are transported to the interface, where they break the hydrogenated silicon bonds creating a hydrogen molecule and a trivalent silicon defect, the interface trap.

Figure 2 shows a schematic energy band diagram of a MOS device indicating the main processes leading to the build-up of surface damage induced by radiation.

2.2 Effects of Radiation-Induced Damage on MOS Devices

2.2.1 Threshold Voltage Change

Charges present in the oxide or at the Si-SiO₂ interface cause an overall shift of the C-V characteristics as shown in Figure 3. Curve a) represents the ideal MOS C-V curve. Curve b) shows a parallel shift due to fixed-oxide charge, mobile ionic charge and oxide-trapped charge present in the SiO₂. Additionally, for a high density of interface-trapped charges the curve as illustrated by Figure 3, will be parallel shifted and distorted due to the dependency of the interface-trapped charge density on the surface potential. For the nMOS capacitor, an increase of the threshold voltage will be observed with an increasing density of the radiation-induced charges.

2.2.2 Increase of Leakage Current

A build-up of radiation-induced interface-trapped charge causes an increase of the surface recombination velocity. This leads to larger surface generation cur-

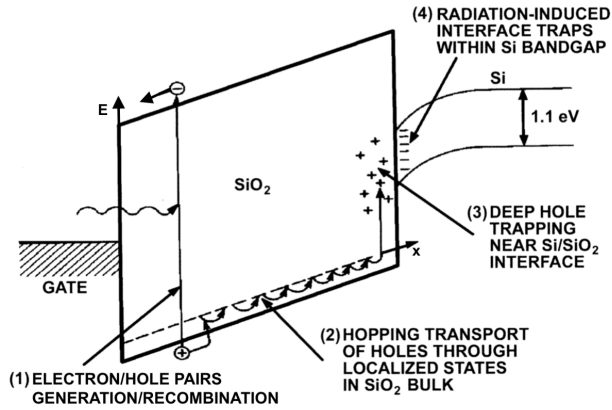


Figure 2: Schematic energy band diagram of a positive biased MOS device, indicating the main processes leading to radiation-induced surface damage. Figure adopted from [31].

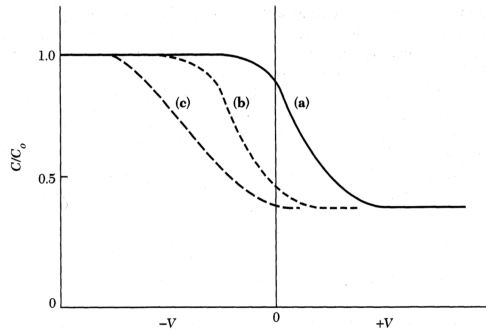


Figure 3: Effect of oxide charges and interface traps on the MOS C-V curve: a) Ideal MOS C-V curve, without oxide charges. b) Parallel shift of the curve due to fixed-oxide charge, mobile ionic charge and oxide-trapped charge present in SiO_2 . c) Parallel shift and distortion of the C-V curve due to interface traps. Figure adopted from [32].

rents and thus to a higher leakage current with increasing dose [33]. The increased leakage current will consequently increase the dark current in the detector. The dark current level in the sensor is a crucial characteristic as it impacts many operational parameters of the detector, e.g. noise, dynamic range, and others. A detailed discussion on the detector parameters and the role of leakage current will be discussed in the following chapters.

2.2.3 Decrease of Charge Transfer Efficiency

The radiation-induced charges at the Si-SiO₂ interface act like trapping centres. This effect is very important for charge-coupled devices (CCDs). A charge resulting from a photon interaction has to be transferred through many channels (pixels, where each pixel represents a MOS capacitor) to read out a CCD detector (based on MOS). If part of the charge is trapped during the transfer at the readout node, a lower charge than expected will be measured. The parameter measuring the charge losses in a CCD device is the so-called charge transfer efficiency (CTE), i.e. a ratio of charge transferred between two neighbouring pixels to the total amount of charge contained in the pixel before the transfer

$$CTE = \frac{Q_{n+1}}{Q_n}. \quad (1)$$

Increased charge trapping hence decreases the CTE [33], and this reduction will lead to an inaccurate representation of the measured quantities, e.g. wrongly measured energy of the incoming radiation.

2.2.4 Decrease of Breakdown Voltage

As experimentally observed by Blackburn et al. [34] and Pugh et al. [35], the breakdown voltage of a MOSFET is strongly affected by ionizing radiation. The breakdown voltage is significantly decreased with increasing total radiation dose for both n- and p-channel devices. It was also shown that the response of the breakdown voltage on the total dose depends on the method used to optimize the pre-radiation breakdown voltage [35].

2.2.5 Decrease of Charge Carrier Mobility

The charge carrier mobility degrades with increasing radiation dose. The mobility of charges is vital for the detectors operated at high frame rates, e.g. 4.5 MHz detectors at the EuXFEL (see Table 1) as the collection of the radiation generated charges has to happen within nanoseconds. Consequently, the decreased charge mobility may result in incomplete charge collection within the integration window of the detector and hence lead to wrongly measured quantities. Sexton and Schwank [36] showed that the mobility decreased is caused by a build-up

of interface-trapped charge, which is induced by radiation. Schwank et al. also showed that the decrease of charge carrier mobility does not depend on the density of the oxide-trapped charge.

2.3 Detector Performance Parameters Relevant for Radiation Damage

The detector performance parameters that are used to characterize the quality of the data produced by the detector can also be used to indicate radiation-induced damage. The parameters evaluated in the radiation damage study are presented in the following.

2.3.1 Dark Signal

The dark signal S_d results from a detector signal when the detector is not exposed to any radiation. It has two contributors, i.e. the dark current and the pedestal. The dark current I_{Dark} is due to a current I_t induced by thermally generated electron-hole pairs and an additional leakage current I_l resulting from, e.g. radiation-induced damage, i.e.

$$I_{\text{Dark}} = I_t + I_l \quad (2)$$

Ranuárez et al. [37] discuss different components of the leakage current, the models and mechanisms, also involving the role of the radiation-induced interface traps, are presented by Nathan and Das [38] and by Larcher et al. [39].

The pedestal P as used in this thesis is a baseline value generated by detector electronics for its proper functioning, e.g. to avoid negative values at the Analog-to-Digital Converter (ADC) or shift the signal values to a specific ADC range. The contribution of the thermally generated charges can be efficiently decreased by cooling the detector's sensor.

The two parameters associated closely with the dark signal are offset and noise. In general, offset is the average value of the dark signal integrated by the detector, i.e.

$$\text{offset} = \frac{1}{N} \sum_{i=1}^N (I_{\text{Dark}} + P). \quad (3)$$

The detector's noise represents variations of the dark signal, which are due to contributions of different noise sources, e.g. noise from readout electronics (marked as readout), thermal noise, leakage current variations, and so on. The noise observed at the detector is a superposition of all the contributing sources. A superimposed noise observed for a given detector is usually evaluated by an equivalent noise charge (ENC) given in units of e^- or eV . It is given as

$$ENC_{\text{tot}} = \sigma_{\text{tot}} = \sqrt{\sigma_{\text{Thermal}}^2 + \sigma_{\text{Leakage}}^2 + \sigma_{\text{Readout}}^2 + \dots} \quad (4)$$

As explained in previous chapters, the radiation-induced damage often induces an increase in the leakage current. Since the leakage current is a contributor to the dark current, its increase will affect both the offset and noise parameters, as shown above. Consequently, the change observed on the offset and noise can be directly linked to the radiation-induced damage, assuming no changes were applied to the sensor or the electronics setup.

2.3.2 Dynamic Range

The dynamic range of a detector determines its ability to detect low-intensity signals alongside high-intensity signals. In detector systems, where the measured analog quantity is digitized by ADC, the upper limit is given by the maximal signal the ADC can resolve. The dynamic range is hence given as

$$DR = \frac{\text{Max. signal (e}^-)}{\sigma_{\text{tot}}}. \quad (5)$$

As shown in the equation above, the dynamic range represents the signal-to-noise ratio (SNR) for the highest detectable signal, if contribution of the background to the signal is negligible. The lower limit of the dynamic range is determined by the noise of the detector. However, in the detector community, the dynamic range is often understood as the number of ADC levels available for photon detection. The resolution of the ADC M is usually expressed as bit depth, which represents the number of signal quantization levels

$$N = 2^M, \quad (6)$$

which gives a limit to the maximal signal. As explained before, the detector offset is always present in the measured signal, thus acting as a lower limit of the available range of values. Taking the offset as "background" (denoted as "bg"), the number of available levels N_A for our measurement is

$$N_A = N - bg, \quad (7)$$

which may then be used to describe the dynamic range of the ADC. This approach is justified if the noise is small in comparison to the overall signal. In the previous section, we have discussed the relation between the leakage current and the detector offset. Analogously, if the offset rises due to radiation-induced leakage current increase, the dynamic range decreases. Hence, we can talk about dynamic range reduction R_{DR} , which can be defined as

$$R_{\text{DR}} = \frac{\Delta bg}{N_A}, \quad (8)$$

$$\text{and } \Delta bg = bg_{\text{post}} - bg_{\text{pre}},$$

where bg_{pre} and bg_{post} are offset values before irradiation of the detector, respectively after irradiation.

2.3.3 Energy Resolution

The energy resolution of a detector determines its capability to distinguish photons with different energies. If one considers mono-energetic photons, the number of generated charges will oscillate around the mean value

$$\langle N \rangle = \frac{E}{w}, \quad (9)$$

where w is the mean energy needed to create an electron-hole pair (3.65 eV for Si [32]) and E is the energy of the incoming photon. This signal oscillation is due to statistical fluctuations in the excitation and ionization processes inside the sensor material. Assuming the charge creation is an independent random process (describable by Poisson statistics), according to the central limit theorem, the distribution of a sum of a large number of independent variables (generated charges) converges to a normal distribution. Therefore, a Gaussian distribution is often a good description of the shape of a photo-peak with the Full Width at Half Maximum (FWHM) denoting the energy resolution. The measured FWHM of the photo-peak is generally used to describe the energy resolution of a detector. However, as described by U. Fano [40] the energy resolution of a detector is better than described by Poisson statistics as part of the absorbed energy does not invoke ionization but is used for other processes as e.g. lattice vibrations. Hence the process of charge creation is not purely random. The coefficient describing the deviation from Poisson statistics is known as Fano factor F , and it is a material-specific constant. For silicon it amounts to $F = 0.115$ [41]. The energy resolution of a detector is then given as

$$FWHM = 2.355 \times w \sqrt{\frac{FE}{w}}, \quad (10)$$

where F is the Fano factor. Additionally, the contribution of the detector noise to the energy resolution has to be considered, yielding

$$FWHM = 2.355 \times \sqrt{RMS^2 + FEw}, \quad (11)$$

where RMS (root-mean-square) is the detector noise expressed in eV.

As the energy resolution is also a function of noise, it is expected that a noise increase due to radiation-induced damage will also impact the energy resolution of the detector, resulting in a broadening of the photo-peak.

2.3.4 Signal-To-Noise Separation

Often, experimental applications (e.g. low energy spectroscopy experiments, imaging experiments) require a detector with single-photon sensitivity, i.e. the capability to resolve single photons from noise. A common requirement for imaging detectors used at FEL facilities is a false hit detection probability per megapixel area, e.g. less than one false hit per million of pixels per image. This approximately corresponds to a photon peak-to-noise separation of 5σ at a certain energy. The lowest acceptable signal-to-noise value is usually considered to be 3σ , which corresponds to ≈ 2700 false hits per million pixels. In this context, the detector's noise and the peak width are important performance parameters, which, as already shown, both increase with radiation-induced damage.

2.3.5 Absolute Gain

In the case of an energy or intensity resolving detector, a relation converting the measured signal into a physical quantity, i.e. energy, is needed. The electrical signal created inside the sensor is amplified, shaped and digitized by the detector electronics. The detector provides output in digital units, so-called Analog Digital Units (ADU). The factor converting the digital unit at the detector output to the physical energy unit at its input is known as absolute detector gain. It is determined by the detector's amplification and digitization stages. The existence of an absolute gain as a conversion coefficient between energy and ADU units is justified when related purely to the measured photo-peak, neglecting the secondary effects of photon redistribution to lower channels, e.g. due to Compton scattering, escape peaks due to internal fluorescence in the sensor material, backscattering¹ or other processes related to photon interactions with matter (see e.g. Knoll [42]). Potential changes of the absolute gain due to radiation damage may suggest damage to other detector components, e.g. the pre-amplifier or ADC.

3 Dissertation Thesis Aims

The main goals of the dissertation thesis can be arranged to the following points:

1. Description of detector parameters, from which radiation damage effects could be estimated and introduction of the tools to analyze and characterize radiation induced effects.
2. Radiation hardness tests of the ePix100a detector in the EuXFEL radiation environment. The detector is important for the scientific operation of the

¹Compton scattering of the incoming photons with the material surrounding the detector at an angle $> 90^\circ$.

facility. Since it has not been built explicitly for the EuXFEL needs, its tolerance to FEL radiation has not been assessed before.

3. Calculation of the absorbed dose during the observation duration, to analyse impact of the dose to detector components.
4. Understanding the observed radiation damage effects for a specific sensor design.
5. Evaluation of the dose limit reducing the detector operation parameters to such extent that they no longer meet pre-requirements for reliable scientific data production.
6. Estimates on the lifetime of EuXFEL detector systems based on the conducted experiments.

4 Experiment Methodology

4.1 The ePix100a Detector

The ePix100a is a backside illuminated low noise camera optimized for X-ray experiments requiring high spatial resolution and signal-to-noise ratio in the energy range between 2 keV and 18 keV [43].

The ePix100a detector module comprises four ASICs flip-chip bonded to a $500\ \mu\text{m}$ thick silicon sensor with pixels of $50 \times 50\ \mu\text{m}^2$, the front-end electronics, the cooling system, its mechanics and housing. It is a 0.5 Mpixel camera with 704×768 pixels. A summary of the main ePix100a characteristics is given in Table 1.

The left panel of Figure 4 shows a schematic view of a vertical cross-section of the ePix sensor. The backside plane made from aluminium acts as the photon entrance window. The bulk of the sensor is made of p-doped high resistivity silicon with a phosphorus implanted backside (n^+) and a boron implantation at the side of the metal gates (p^+) to create a low resistance contact. Solder bump bonds provide a connection to the ASIC. The $500\ \mu\text{m}$ thick sensor enables the detection of X-ray photons with energies between 3 keV and 13 keV with a quantum efficiency $\geq 80\%$ and at the same time efficiently shields the underlying ASIC from X-ray radiation. Due to its backside-illuminated design, sensor structures sensitive to radiation-induced surface damage (e.g. Si/SiO₂ interfaces) are effectively shielded by the sensor in this energy range.

The ePix100a's ASIC provides signal processing and readout to an array of $352\ \text{pixels} \times 384\ \text{pixels}$. The dynamic range of the camera is equal to $220\ \text{ke}^-$ which is equivalent to $\approx 100 \times 8\ \text{keV}$ photons per pixel. The ePix100a can be operated at a maximum frame rate of 240 Hz. At the EuXFEL, the camera

is operated at 10Hz (train repetition rate). A low noise charge sensitive pre-amplifier (CSA) with pulsed reset processes the analog signal provided by the sensor, which is subsequently low pass filtered. Next, a correlated double sampling (CDS) stage performs a baseline correction and noise reduction of the signal. Finally, the corrected signal is stored in a buffer. Further processing of the analog signal is organized in a column-parallel fashion. Each ASIC is divided into four banks. The analog output of the pixels of one bank accommodates 96 columns. Columns of each bank are multiplexed to a single analog output and subsequently digitized by an external sigma-delta Analog to Digital Converter (ADC). Figure 4 on the right schematically illustrates a structure of the ePix100a readout. The analog output nodes are arranged on the top and bottom sides of the ASICs and sensor. For a detailed description of the ePix ASIC, detector design and a performance review, the reader is referred to Markovic et al. [18], Blaj et al. [43] and Nishimura et al. [44].

The ePix100a module under study was specifically dedicated to perform the radiation-induced damage study. The module has two ASICs with a good noise performance, one ASIC exhibiting significantly higher noise and one unresponsive ASIC. For the purpose of this study, only the two good ASICs were considered and evaluated. All detector components and structures are identical to the modules used for experimental applications at HED and MID. It is to note that the module under investigation is not expected or required to provide the scientific grade performance. A summary of all the ePix100a performance parameters characterized before the module irradiation is given in Table 2.

Table 2: Summary of the performance characteristics of the ePix100a detector.

| Parameter | t_{Int} | 2 ASICs | ROI |
|--|------------------|----------------|----------------|
| Mean offset (ADU) | 50 | 1589 ± 173 | 1755 ± 113 |
| | 800 | 1595 ± 174 | 1762 ± 113 |
| RMS noise (e^-) | 50 | 40.2 | 37.8 |
| | 800 | 48.4 | 47.1 |
| Gain (ev/ADU) | 50/800 | 69.6 ± 0.5 | 70.1 ± 0.5 |
| Dynamic range ($n \times 8\text{keV}$) | 50/800 | 128 | 128 |
| Energy resolution (eV) | 50 | 594 ± 43 | 641 ± 45 |

4.2 Experiment Setup and Methods

The ePix100a radiation damage experiment conducted at the HED was designed to investigate effects induced by irradiation with the FEL beam. The detector was irradiated with a direct attenuated beam. We have used a beam with a photon energy of 9keV, corresponding to the commonly used energy at the HED

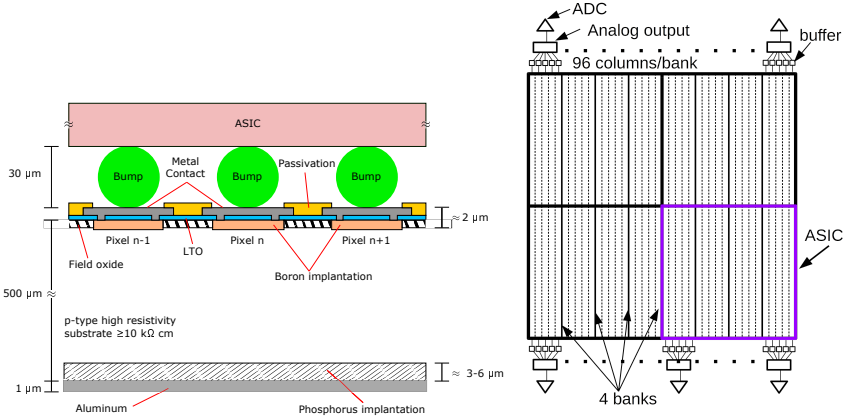


Figure 4: Left: Schematic view of the ePix100a sensor cross-section including interconnection bump bonds and the readout ASIC (kindly provided by M. Kuster). The sensor is illuminated from the backside, i.e. from the bottom. Right: Schematic drawing of the ePix100a sensor showing the arrangement of the 4 ASICs required to read out one sensor section with a size of 352 pixels \times 384 pixels. Each ASIC is divided into four banks accommodating 96 columns multiplexed to a single analog output digitized by an external ADC.

instrument. The full beam energy of the EuXFEL is of the order of mJ. Exposing the detector to the direct beam would cause instantaneous and permanent damage to the detector hardware. We have attenuated the beam below the immediate damage threshold with a configurable stack of Chemical Vapour Deposition (CVD) diamond and Si foils of various thicknesses to avoid the mentioned scenario. An X-ray Gas Monitor (XGM) was continuously monitoring the beam intensity. The XGMs are designed to perform a non-invasive measurement of the X-ray pulse energy with an absolute accuracy of 7% – 10%. A detailed description of the XGM is provided by Sorokin et al. [45], and performance details and an overview of usage scenarios at the EuXFEL are given by Maltezopoulos et al. [46].

Throughout the course of the experiment, we have operated the detector under vacuum at a pressure of 1×10^{-5} mbar, cooled to -9°C and biased with 200 V. The beam spot area was approximately 1 mm^2 , covering an area of ≈ 20 pixels \times 20 pixels of the ePix100a sensor. The beam spot was placed in the area having the lowest pre-irradiation noise, referred to as region of interest (ROI). A summary of the FEL beam settings and detector parameters is given in Table 3.

We have performed the ePix100a irradiation in cycles. Each irradiation cycle consisted of a 20 minutes exposure with a direct FEL beam, followed by dark

Table 3: Summary of the relevant beamline and detector operation parameters as used during the irradiation experiment.

| Beam parameters | |
|---|---|
| Average beam energy at the detector | 10 nJ/Pulse |
| Photon energy | 9 keV |
| Number of X-ray pulses per train | 100 Pulses |
| Dose rate at the Si/SiO ₂ interfaces | 180 kGy/h |
| Beam intensity monitoring | XGMs at HED beamline |
| Detector parameters | |
| Pixel size | 50 μm \times 50 μm |
| Sensor size | 704 pixels \times 768 pixels |
| Sensor thickness | 500 μm |
| Irradiated sensor area | 20 pixels \times 20 pixels (1 mm ²) |
| Full well capacity | 220 ke ⁻ |
| Frame rate | 10 Hz |
| Integration time | 50 μs and 800 μs |
| Bias voltage | 200 V |
| Sensor temperature | -9 $^{\circ}$ C |
| Environment | Vacuum, $p \leq 1 \times 10^{-5}$ mbar |

image measurements with 50 μs and 800 μs long integration times. We used the dark measurements to monitor the state of the detector module after each irradiation cycle. We have irradiated the sensor with a dose rate of approximately 180 kGy/mm²h at the Si/SiO₂ interfaces in the sensor. In total, we repeated the irradiation cycles 15 times during the course of the study.

The experiment further involved calibration data taking prior to and after irradiation to evaluate the performance evolution of the detector. The taken calibration data consists of flat-field measurements using Cu-K fluorescence photons resulting from the irradiation of a 50 μm thick Cu target, taken at 50 μs integration time. The energy of Cu fluorescence photons is $E_{\text{K}\alpha_1} = 8047.78$ eV and $E_{\text{K}\alpha_2} = 8027.83$ eV. The detector was placed at an angle of 90 $^{\circ}$ with respect to the beam, slightly shifted off the beam axis, and a Cu target was installed in a transmission geometry. This detection geometry yielded a detector illumination with additional 9 keV photons originating in the FEL beam due to scattering of the beam on the target material.

4.2.1 Dose Evaluation

The intensity of the beam measured by an XGM does not provide information about the spatial distribution of the beam intensity on the ePix's sensor. In order

to determine the intensity profile of the beam, we have performed measurements of the beam profile at low X-ray intensities with the ePix100a detector. Irradiating the detector with a high beam energy of ≈ 65 pJ led to saturation of the signal. Pixels located in the core of the beam became unresponsive during the time of irradiation. The size of the resulting unresponsive area is approximately equal to the size of the ROI, i.e. $20\text{pixel} \times 20\text{pixels}$. This allows to monitor the position of the beam during each irradiation cycle on the ePix100a sensor, thus allowing for a more precise calculation of the per-pixel dose.

The procedure starts with the evaluation of the position of the inactive pixel area. The Canny edge detection algorithm [47] is employed to detect the edges of the inactive area and assigns a circle to it. The detected circle's centre is assumed to be the beam core's centre. The inactive area is marked with light blue dots, and the white cross corresponds to its centre. Based on the detected circular area, a proportional per-pixel beam distribution $F_{x,y}$ is applied, calculated as

$$F_{x,y} = \frac{E_{B_{x,y}}}{\sum E_{B_{x,y}}}, \quad (12)$$

where $E_{B_{x,y}}$ is the beam energy deposited in a given pixel. The pixel with the highest value from the proportional beam distribution is identified as the circle's centre. In the next step, the XGM intensity is converted to photon count numbers N_{ph} and distributed into the inactive area based on the given proportionality. This procedure is repeated for every image taken during irradiation. The result is the number of photons delivered to a given pixel denoted as photon intake $C_{\text{ph}_{x,y}}$

$$C_{\text{ph}_{x,y}} = \sum_{z=0}^{n-1} (N_{\text{ph}_z} \cdot F_{x,y}). \quad (13)$$

To estimate the absorbed dose, the MULASSIS tool [48] was used to simulate the dose at different depths of the ePix100a sensor. It is a Geant4 [49] based Monte Carlo simulation tool used to analyse particle fluence and dose in various shielding materials. The dose deposited in the ePix100a sensor was simulated by using 13 layers representing the vertical structure of the sensor as shown in Fig. 4, namely: $1\ \mu\text{m}$ Al, $10 \times 50\ \mu\text{m}$ Si, $2\ \mu\text{m}$ SiO₂ and $30\ \mu\text{m}$ Sn. The per-layer simulated dose normalized to $1\ \text{photon}/\text{cm}^2$ was combined with the already calculated spatial photon distribution integrated throughout all irradiation cycles yielding a per-pixel dose profile shown in Figure 5.

5 Results

5.1 Immediate Effects

We have irradiated the ePix100a sensor with a beam attenuated below the immediate damage threshold to maximize the delivered dose. The beam intensity

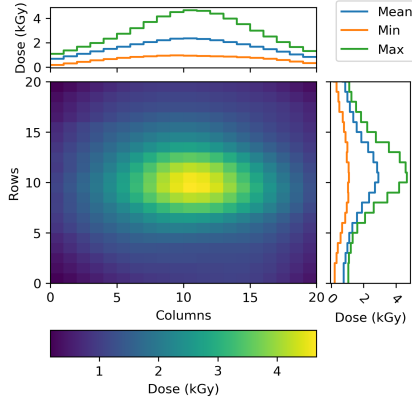


Figure 5: The per-pixel dose distribution deposited at a depth of the SiO_2 layers in the region of interest (ROI).

threshold was tested on a noisy ASIC. We have determined that the ePix100a module can withstand intensities with an energy of up to $E_B \geq 1 \mu\text{J}$ for longer periods of time in the order of minutes. Hence this intensity was used for the module irradiation. Irradiation of the sensor with this intensity caused pixels in the centre of the $20 \text{ pixels} \times 20 \text{ pixels}$ large ROI to become unresponsive. Despite their unresponsiveness during irradiation, these pixels were fully functional during the dark signal measurements.

After each irradiation run, the dark data collected exhibited an increasing number of individual pixels with their offset surpassing the upper level of the ADC dynamic range. Figure 6 shows the behaviour of pixels shortly after the last irradiation. Most of the area shown has pixels completely saturated with a signal (visualized in yellow colour). A potential explanation of the offset exceeding the dynamic range of the ADC is the mechanism suggested by Schwandt et al. [10]. The generation of electron–hole pairs close to the Si– SiO_2 interface and build-up of positive charge lead to high electric fields near the interface, causing changes to the depletion boundary. Coulombic repulsion between positively doped boron implantation and positive charges accumulating near the oxide layer might result in the shrinking of the boron implanted region on its edges, thus exposing the metal contact. The distorted boron-doped region allows the depleted area to extend to the region close to the metal contact. Potentially, the bending of the depletion boundary can reach the edges of the metal contact and thus increase the electron leakage current. When the generation of new charge carriers is interrupted, the recombination process dominates. Hence, the leakage current will decrease exponentially as observed and shown in the right part of Figure 6.

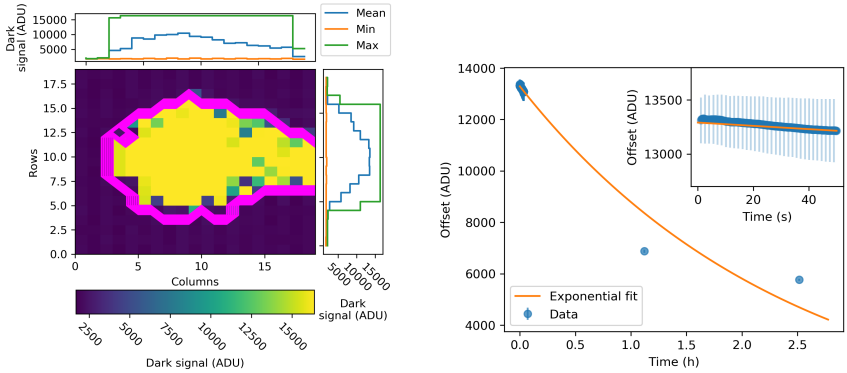


Figure 6: Left: Irradiated sensor area demonstrating saturated pixels with a dark signal above the dynamic range of the ADC. Right: An exponential decrease of the dark signal in a span of three hours after the irradiation.

5.2 Post-Irradiation Performance

5.2.1 Offset and Noise

During the first three hours following the last irradiation cycle the offset of individual pixels decreased exponentially with time with a decay constant of -0.413 h^{-1} as shown in the right part of Figure 6 for $t_{\text{Int}} = 800 \mu\text{s}$.

The offset stabilized three days after irradiation at a higher level of 1832 ADU in comparison to the pre-irradiation level of 1762 ADU. As apparent from Figure 7, the level of offset and noise change measured 3 days after irradiation remains the same also for the consecutive days. In general we observe a larger offset and corresponding ENC increase for $t_{\text{Int}} = 800 \mu\text{s}$.

Evaluating the offset change 46 days after irradiation, yielded an offset increase by approximately 15% for $t_{\text{Int}} = 800 \mu\text{s}$ and by 1% for $t_{\text{Int}} = 50 \mu\text{s}$. As shown in the right part of Figure 7, the RMS noise observed in these pixels follows the same behaviour. While the noise at $t_{\text{Int}} = 800 \mu\text{s}$ has increased by 85%, for $t_{\text{Int}} = 50 \mu\text{s}$ the increase is at the level of 30%.

The measured increase in offset scales linearly with the integration time, i.e. with a factor of $800 \mu\text{s} / 50 \mu\text{s} = 16$, which is expected if the effect is caused predominantly due to an increase of the dark current. As shown in Figure 8, the ratio of offset change for the two integration times approaches the expected factor of 16 when the leakage current increases, which happens for doses above $\approx 4 \text{ kGy}$. The function qualitatively modelling the data consists of three regions describing the expected behaviour of the offset with different integration times. The first region, constant at one, expresses negligible contribution of the leakage current (dose = 0 Gy), hence no difference between shorter and longer integration

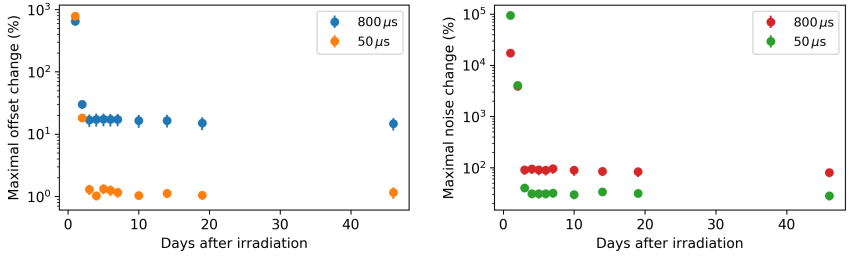


Figure 7: Left: Evolution of the offset as observed in the pixel showing the highest relative offset change for the two integration time settings, i.e. $t_{\text{Int}} = 50 \mu\text{s}$ and $t_{\text{Int}} = 800 \mu\text{s}$. A stabilized state at increased offset values (with respect to the pre-irradiation offset level) follows the exponential decrease of the offset observed during the first days. Right: Relative change of the noise as observed during the days following the last irradiation cycle. The noise behaviour as a function of time mirrors the time evolution of the offset.

time exists. As the dose increases, the leakage current exhibits an increase (the second region). Finally, it approaches the third region at a value of 16, which is expected when the leakage current dominates.

The spatial distribution of the induced offset (left) and noise (right) changes 46 days after irradiation is shown in Figure 9 for $t_{\text{Int}} = 800 \mu\text{s}$.

Since different pixels within the ROI have received a different dose and assuming the pixels inside the ROI react similarly to radiation-induced damage, we can evaluate the change of the offset and RMS noise between pre- and post-irradiation conditions depending on the dose. As the design of the pixels is the same, and minor variations in the sensor production process can be neglected, this assumption is justified.

Figure 10 shows the offset (left) and noise (right) changes depending on the absorbed dose at the depth of the SiO_2 interface as measured 46 days post-irradiation. Here the influence of the longer integration time is clearly visible. The slope derived from fitting a linear function to the data yields an offset and ENC change rate of $(56.0 \pm 0.6) \text{ADU/kGy}$ and $(8.7 \pm 0.1) e^-/\text{kGy}$ for $t_{\text{Int}} = 800 \mu\text{s}$ and $(1.0 \pm 0.2) \text{ADU/kGy}$ and $(2.0 \pm 0.1) e^-/\text{kGy}$ for $t_{\text{Int}} = 50 \mu\text{s}$, respectively.

If absorption of the radiation in silicon is neglected when calculating the dose, the offset and ENC change rate yields $(235.9 \pm 2.6) \text{ADU/MGy}$ and $(37.4 \pm 0.6) e^-/\text{MGy}$ for $t_{\text{Int}} = 800 \mu\text{s}$ and $(4.2 \pm 0.6) \text{ADU/MGy}$ and $(8.3 \pm 0.4) e^-/\text{MGy}$ for $t_{\text{Int}} = 50 \mu\text{s}$. The maximum observed increase of the offset reduces the available dynamic range of the detector by approximately 2% for $t_{\text{Int}} = 800 \mu\text{s}$ and $\approx 0.1\%$ for $t_{\text{Int}} = 50 \mu\text{s}$.

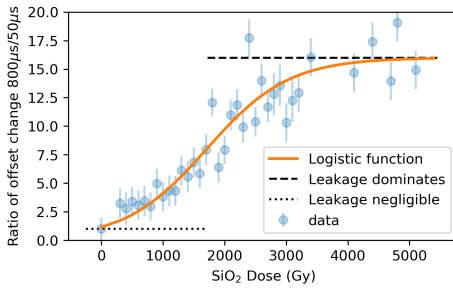


Figure 8: Ratio of the offset change measured at $800\mu\text{s}$ and $50\mu\text{s}$ (blue dots). The black line shows the scaling factor of 16 expected from the ratio of the integration times. The ratio of offset change for the two integration times approaches the expected factor of 16 when the leakage current contribution dominates, which happens for doses above $\approx 4\text{kGy}$.

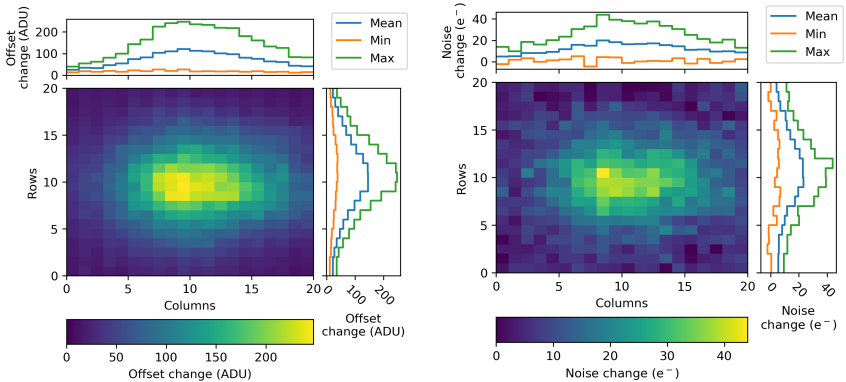


Figure 9: Radiation-induced changes of the offset (left) and noise (right) for $t_{\text{Int}} = 800\mu\text{s}$ evaluated 46 days after irradiation.

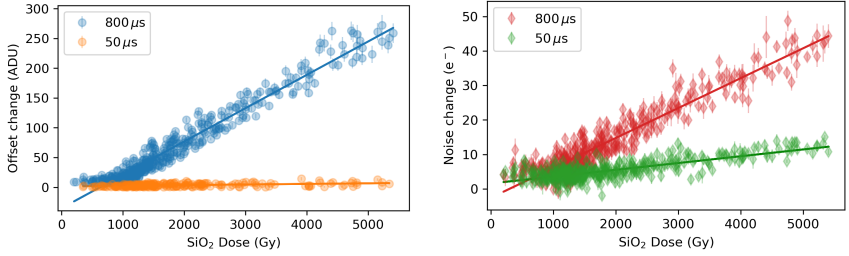


Figure 10: Left: The offset change observed in pixels of the ROI (difference between pre- and post-irradiation values) depending on the accumulated dose at the depth of SiO_2 layers is shown for $t_{\text{Int}} = 50 \mu\text{s}$ (orange) and $t_{\text{Int}} = 800 \mu\text{s}$ (blue). Right: Dependency of the ENC observed in pixels of the ROI on the accumulated dose in units of electrons for the same integration times (green: $50 \mu\text{s}$, red: $800 \mu\text{s}$).

5.2.2 Gain and Energy Resolution

In order to characterise the gain and energy resolution of the ePix100a after irradiation, we took post-irradiation Cu-fluorescence flat-field data. The data taking took place approximately one and a half hours after completion of the last irradiation cycle. At that time, most of the pixels in the central part of the ROI were still saturated, thus not detecting the charge created by a photon interaction. Due to time-constrained access to the instrument and beam, performing calibration measurements at a later time was not possible. Therefore, we have used pixels located in the periphery of the saturated area to compare the pre- and post-irradiation performance of the gain and energy resolution.

Figure 11 on the left shows a comparison of the measured spectrum of the $\text{Cu-K}\alpha$ line blend and the 9keV line before (black) and after irradiation (red). The spectrum was calculated from periphery pixels in the ROI. The FWHM of the lines is larger after irradiation, and the lines have a more pronounced low energy tail.

The right plot of Figure 11 shows the relation of FWHM on the dose accumulated by each pixel. We observe an increase of the FWHM at the level of $(115 \pm 71) \text{eV/kGy}$. Following the Fano statistics-driven energy resolution of a detector described in section 2.3.3, an expected energy resolution can be calculated based on the measured noise. The yellow squares (labelled as "Calculated") refer to values calculated as given by Equation 11. The increase of the FWHM values follows the same slope (within the estimated errors) as the calculated intrinsic resolution values. The intercept values of the linear models are separated by $(267 \pm 82) \text{eV}$, which is approximately consistent with the mean noise of peripheral pixels measured after irradiation, i.e. $(167 \pm 87) \text{eV}$. These results sug-

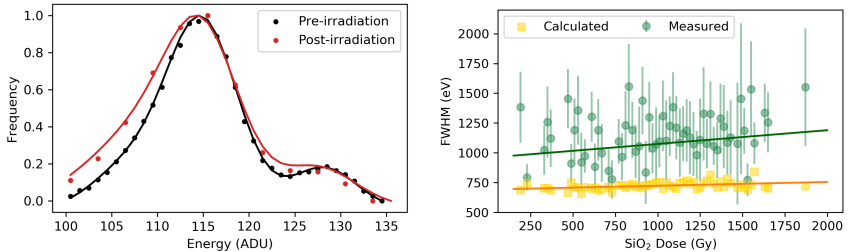


Figure 11: Left: The spectral distribution of the Cu-K α photons and 9keV photon peak (detected by pixels in the periphery of the ROI) before irradiation (black) and after irradiation (red). Right: The Cu-K α peak width (assessed as FWHM) depending on the dose absorbed in the SiO₂ layer. Values extracted from the measurement are marked with green dots, while the yellow squares shows the expected FWHM values calculated from the noise.

gest that a radiation-induced noise increase drives the observed broadening of the Cu-K lines.

As the flat-field calibration measurement contained only pixels with an absorbed dose below 2kGy, we could not evaluate the behaviour of the gain for the most irradiated pixels.

In order to identify potential gain changes, we performed a charge injection scan with the current sources implemented in each pixel 240 days after irradiation. Furthermore, performing a charge injection scan allows separating different sources for the potential gain changes. Following the sensor and ASIC layout shown in Figure 4, we can identify two sources for the observed effect, radiation damage induced in the sensor and the readout electronics located in the ASIC. During this scan, an increasing amount of charge is injected into the pre-amplifier with an internal 10-bit pulser, thus simulating the charge created by photon interactions in the sensor material. In this mode, the sensor does not contribute to the measured signal. We used 1024 steps of the pulser to scan the full dynamic range of the ADC. Gain values depending on the absorbed dose calculated from Cu-K fluorescence data are shown on the left panel of Figure 12. The plot shows only gain values for doses below 2kGy. The slope $(-4.6 \pm 5.7) \times 10^{-5} \text{ ADU keV}^{-1} \text{ Gy}^{-1}$ derived from a linear model fitted to the data is consistent with zero. This indicates that the gain does not change significantly up to a dose of ≈ 2 kGy. This behaviour changes as soon as higher dose levels were reached. Taking the charge injection data covering the range between 3500Gy and 5500Gy into consideration (right part of figure 12), we find the gain decreasing with the rate of $(-7.4 \pm 0.5) \times 10^{-5} \text{ ADU keV}^{-1} \text{ Gy}^{-1}$ as indicated by the black line in the right panel of Figure 12. Based on the estimated slope we expect a gain decrease by 1 ADU/keV per ≈ 13.5 kGy. The observed gain

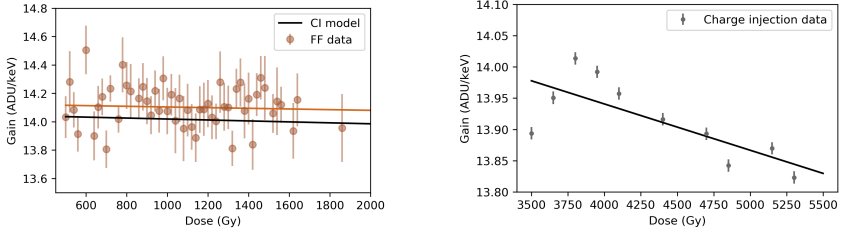


Figure 12: Left: Gain estimated from the Cu-K fluorescence data depending on dose. The black line shows a model derived from charge injection data (marked as "CI model") extrapolated to the dose range of (500 – 5500) Gy. Right: The gain calculated from the internal charge injection data in relation to the absorbed dose is shown. Only gain values for a dose above 3.5 kGy were evaluated.

decrease determined from the charge injection data indicates damage occurring on the readout electronics in the ASIC.

5.3 Lifetime Estimates

I have used the radiation-induced damage presented in the previous to estimate the lifetime of the detector depending on the beam energy used during experiments and limits for the measurement time beyond which the performance of the detector will significantly degrade. The estimates presented in the following are based on the extrapolation of the measured relationship of the induced damage and dose absorbed in the SiO₂ layer.

Figure 13 illustrates the time needed to reduce the dynamic range depending on the beam energy. A reduction of the dynamic range by 50% can be expected at a dose of ca. 131 kGy for $t_{\text{Int}} = 800 \mu\text{s}$ and at ca. 7.4 MGy for $t_{\text{Int}} = 50 \mu\text{s}$ deposited in a single pixel. This amounts to ca. 13 MGy for $t_{\text{Int}} = 800 \mu\text{s}$ and 740 MGy for $t_{\text{Int}} = 50 \mu\text{s}$ of dose deposited in the SiO₂ layer per 20 pixels \times 20 pixels area (ROI), assuming a per-pixel beam distribution obtained during radiation damage study. Saturation of the ADC dynamic range will occur at 262 kGy ($t_{\text{Int}} = 800 \mu\text{s}$), respectively at 14.8 MGy ($t_{\text{Int}} = 50 \mu\text{s}$) for a single pixel, i.e. at 26 MGy ($t_{\text{Int}} = 800 \mu\text{s}$) and at 1.48 GGy ($t_{\text{Int}} = 50 \mu\text{s}$) of the total absorbed dose in the ROI. The left panel of Figure 13 shows three exemplary cases for the expected dynamic range behaviour: a dynamic range reduction as observed in this radiation damage study (blue dots), an extrapolated loss of 50% of the ADC range (orange dots) and the saturation of the ADC dynamic range due to the leakage current (green dots) for 800 μs integration time. The same cases are plotted for $t_{\text{Int}} = 50 \mu\text{s}$ on the right. The lowest beam energy shown in both graphs corresponds to an energy equivalent to the upper limit of the ePix100a dynamic range, i.e. 100 photons at 8 keV. We assumed that mostly the same region

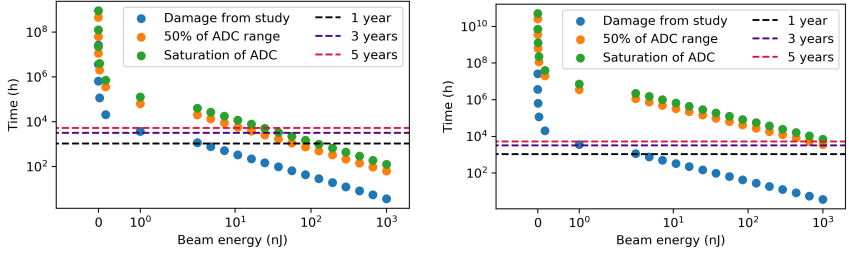


Figure 13: Estimate of time needed to reach specific level of the dynamic range reduction at a certain beam energy. Three scenarios are shown; the reduction level observed during this radiation damage study (blue dots), reduction to 50% of the initial dynamic range (orange dots) and complete saturation of the ADC by the leakage current (green dots). The left plot shows the estimate for $t_{\text{Int}} = 800 \mu\text{s}$ and the right plot is for $t_{\text{Int}} = 50 \mu\text{s}$.

of the detector is illuminated during scientific experiments for the estimate. This assumption is reasonable for small-angle scattering experiments. The horizontal lines in both plots visualize the number of hours the detector can be exposed to the beam during one, three and five years of operation at the EuXFEL to reach the corresponding dynamic range reduction. For our estimate, we assumed 4216 hours of beam time operation per calendar year at the EuXFEL. This value corresponds to the planned X-ray delivery time for the year 2021. As one beamline serves two scientific instruments, the allocated time is shared equally between the two instruments. Moreover, we estimate the detector to be exposed to X-rays only 50% of the available time.

As explained in section 2.3.4, peak-to-noise distinction expressed in the unit of standard deviation is often used as a parameter to evaluate the performance quality of spectroscopic detectors. Figure 14 shows decrease of a separation power below 5σ (cyan) or 3σ (magenta) at 9keV if the detector is exposed to a given beam energy for a specific amount of time. A plot on the left shows the separation power reduction at $800\mu\text{s}$ integration time and the right plot at the integration time of $50\mu\text{s}$. As in the previous figure, the horizontal lines represent hours of exposure referenced to number of beam hours at the EuXFEL per calendar year. A critical noise increase, hence reduction in peak-to-noise separation is only expected with exposure to beam energies above the detector's dynamic range. Irradiating the detector for 2 years with a beam energy of 2.5 nJ would cause a drop below 3σ at $800\mu\text{s}$ integration time, while at $t_{\text{Int}} = 50\mu\text{s}$ the same energy during 5 years would lead to a drop below 5σ .

Table 4 summarizes estimates for SiO_2 dose thresholds above which the detector will demonstrate degraded performance in terms of reduced ADC range or reduction in peak separation strength.

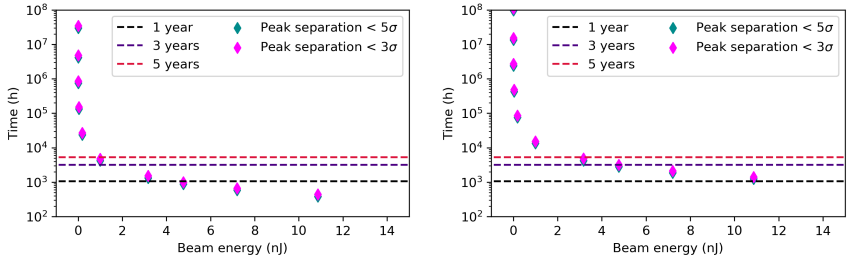


Figure 14: Estimate of time needed to reduce a peak-to-noise separation power below 5σ (green) and 3σ (pink) for $t_{\text{Int}} = 800\mu\text{s}$, shown on the left panel and for $t_{\text{Int}} = 50\mu\text{s}$ shown on the right, in dependency of the used beam energy.

Table 4: Estimate of dose thresholds to experience degraded detector performance in terms of ADC range reduction and reduction in peak separation strength.

| Integration time | Dose absorbed in SiO ₂ | | | |
|------------------|-----------------------------------|----------|-----------------|-------------|
| | ADC range reduction | | Peak separation | |
| | 50 % | 100 % | $< 5\sigma$ | $< 3\sigma$ |
| $50\mu\text{s}$ | 7.4 MGy | 14.8 MGy | 28 kGy | 32 kGy |
| $800\mu\text{s}$ | 131 kGy | 262 kGy | 9 kGy | 10 kGy |

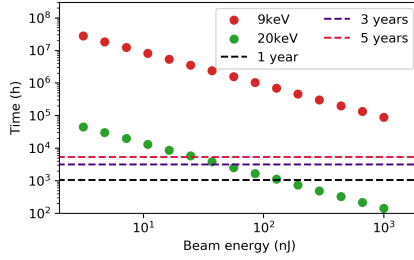


Figure 15: Time estimate for a gain decrease by 1 ADU/keV for the photon energy of 9 keV (red) and the photon energy of 20 keV (green) at certain beam energy. The horizontal lines on the left panel visualize the number of hours the detector can be exposed to the beam during one, three and five years of operation at the EuXFEL to reach the mentioned gain decrease.

The gain depends only weakly on an absorbed dose as above-located metal connections and silicon sensor significantly attenuated the incoming radiation. In the case of higher photon energies, the ASIC will become more susceptible to radiation damage. The same energy deposited by, e.g. 20 keV photons would lead to an absorbed dose which is more than three orders of magnitude higher in comparison to 9 keV. Suppose the induced radiation damage on the readout electronics irradiated with 20 keV photons follows the same relation as observed for 9 keV photons. In that case a comparison for a time range to observe gain decrease by 1 ADU/keV can be made. Figure 15 illustrates the effect of photon energy on the time needed to observe a gain decrease by 1 ADU/keV at a given beam energy.

6 Main Findings and Contributions of the Thesis

- The ePix100a detector was tested for its radiation hardness in the EuXFEL radiation environment. The main goal of the performed experiment was to assess the impact of the FEL irradiation on the performance changes of the detector. Understanding the effects of radiation-induced damage on the detector's performance and assessing the detector's lifetime is essential to ensure reliable scientific operation.
- The study provides relations of essential detector performance characteristics on the dose absorbed at a depth of Si-SiO₂ structures for two integration times, i.e. 800 μs and 50 μs. It was shown that the main effect leading to worsening of the performance parameters is an increase of the

radiation-induced leakage current, which occurs due to the build-up of interface trapped charges at the Si-SiO₂ interface.

- Even though the incoming beam intensity of 9 keV photons was significantly attenuated by 500 μm thick sensor, a weak decrease of the gain as a function of the dose was observed. This is due to damage also induced on the ASIC, more specifically on the pixels' pre-amplifiers. If the photon energy of the beam is to increase, the detector electronics will be more susceptible to damage and hence more significant gain shifts can be expected.
- It is important to provide a time frame for damage compensation measures to occur in terms of re-calibration, repair or module exchange. The time evolution of the parameters necessary for reliable scientific operation, i.e. dynamic range and signal-noise separation with irradiation, are given to address this. The assessment is done by extrapolation of the measured dependencies of the performance parameters on the absorbed dose. The boundary doses above which a degraded performance is expected are also provided.
- The results presented in the thesis are not exclusive to the European XFEL but are relevant and applicable to other facilities.

7 Conclusions and Outlook

I investigated the radiation damage of the ePix100a since its tolerance to FEL radiation has not been assessed before. The detector plays a key role in the scientific program of two EuXFEL instruments, i.e. HED and MID. I introduced the mechanisms leading to surface radiation damage in detectors based on MOS structures and the effects this radiation damage induces. The induced radiation damage effects influence the performance parameters of the detector, i.e. offset, noise, dynamic range, energy resolution, signal-to-noise and gain. Hence, the radiation damage of the ePix100a was evaluated and discussed in connection to these parameters.

The ePix100a detector was irradiated under controlled conditions with the direct and attenuated EuXFEL beam with X-ray photons with an energy of 9 keV and a beam energy of 1 μJ. Pixels irradiated by this energy do not show a signal-dependent response upon irradiation but remain functional under normal operating conditions. The irradiated area of 1 mm² has received a dose of approximately 760 kGy at the depth of Si/SiO₂ in the sensor, which corresponds to 180 MGy delivered to the surface of the sensor.

The offset and noise were evaluated for two integration times, i.e. 50 μs and 800 μs. The integration time of $t_{\text{int}} = 800 \mu\text{s}$ was selected due to the higher sensitivity even to small changes in the leakage current induced by radiation damage,

while $t_{\text{Int}} = 50 \mu\text{s}$ corresponds to a typical integration time used at HED. The dominating source of the noise before irradiation was noise induced by readout electronics, while after receiving $> 4\text{kGy}$ at a depth of SiO_2 , the contribution to the noise due to higher leakage current dominates. Hence I can conclude that the observed increase of the offset and noise is due to an increase of the leakage current. The same can be stated for the observed broadening of the Cu-K fluorescence line measured one and a half hours post-irradiation since the measured FWHM is scaling with the increasing noise observed in the pixels. I have observed a FWHM increase by $\approx 115 \text{eV/kGy}$.

A change of the gain is not expected for a dose $< 4\text{kGy}$. Nevertheless, a charge injection scan showed a slight gain decrease for the most irradiated pixels and suggested weak damage occurring at the pixels' readout electronics. The gain depends on an absorbed dose only weakly as the incoming radiation was significantly attenuated by above-located metal connections and silicon sensor. In the case of higher photon energies, the ASIC will become more susceptible to radiation damage. The same energy deposited by, e.g. 20keV photons would lead to an absorbed dose which is more than three orders of magnitude higher in comparison to 9keV .

The results from the study of detector performance parameters on radiation-induced damage were extrapolated to assess the lifetime of a detector with regards to the impact of the detector parameters and their time evolution with irradiation on reliable scientific operation. Significant reduction of the dynamic range, i.e. $R_{\text{DR}} > 50\%$ is expected if the beam energy deposited in the pixel exceeds the dynamic range of the ADC by at least five orders of magnitude (for $t_{\text{Int}} = 800 \mu\text{s}$). Single-photon discrimination at a level of $> 5\sigma$ can be achieved with the ePix100a up to a dose of 9kGy at $t_{\text{Int}} = 800 \mu\text{s}$ and up to 28kGy at $t_{\text{Int}} = 50 \mu\text{s}$. The results presented in this thesis are not exclusive to the EuXFEL but are of generic nature, thus can be transferred to other use cases and facilities.

In the near future, we plan to investigate the possibility of mitigating the radiation-induced damage and restoring the non-irradiated detector performance by sensor annealing to conclude the ePix100a radiation damage study. In the case of experiencing reversible (non-destructive) radiation damage during scientific experiments, this could potentially cure the module without the need to replace it.

I have shown that the main radiation-induced effect causing change to detector performance parameters is the radiation-induced leakage current. I also have shown that the level of the effect on the detector parameters depends on the integration time of the detector, i.e. the longer the integration time is, the higher increase of offset and noise can be expected. The imaging detectors operated at 4.5MHz have the integration time in the range of tens to hundreds of nanoseconds, e.g. the LPD detector has integration time of 90ns . This is more than 500 times shorter time in comparison to the standard integration time of the

ePix100a. The leakage current contribution to the noise of the LPD is a factor of 100 lower in comparison to the other noise sources [13], which means that in order to observe an increase of the noise caused by the increase of leakage current, the integration time would have to be two orders of magnitude higher. Hence, the radiation-induced damage comparable to the level presented by this study for a 4.5 MHz operated detector can not be characterized by the offset or noise increase. Instead, the effect on the gain, in the case of irradiation with higher photon energies or charge collection efficiency due to charge mobility decrease, could be of interest.

This study proved that the ePix100a could be used without significant degradation of its performance for several years if the deposited energy in a given pixel throughout this time does not exceed 1 nJ. In such a case, the ageing of the detector and its electronics will be driven by other processes than radiation damage effects.

8 Zhrnutie

V mojej práci som sa zamerala na skúmanie radiačného poškodenia detektora ePix100a, keďže detektor zohráva dôležitú úlohu pri experimentálnych meraniach na dvoch experimentálnych staniciach v EuXFEL (HED[3] a MID[4]). Ide o jedinečný a dôležitý výskum v tejto oblasti, keďže doterajšie zdroje neuvádzajú existenciu obnovených meraní.

Vplyv radiačného poškodenia som skúmala vzhľadom na operačné parametre detektora: ofset, šum, dynamický rozsah, energetické rozlíšenie, pomer signál-šum a konverzný faktor. Detektor bol ožarovaný priamym a čiastočne odtieneným röntgenovým laserovým zväzkom, s použitím 9 keV fotónov s energiou 1 μ J. Pixely ožarované takouto energiou zväzku nevykazovali počas merania žiadny merateľný signál. Po ukončení ožarovania však opäť nadobudli svoju funkčnosť.

Ožiarená plocha veľkosti približne 20 pixelov \times 20 pixelov, odhadom 1 mm², absorbovala dávku približne 760 kGy na rozhraní Si/SiO₂, čo zodpovedá približne 180 MGy na povrchu senzora.

Ofset a šum sa vyhodnocovali pre dva integračné časy, a to pre 50 μ s and 800 μ s. Dlhší integračný čas sme zvolili pre jeho vyššiu citlivosť na malé zmeny vo zvodovom prúde senzora a kratší čas je zvyčajným integračným časom používaným pri meraniach.

Pred ožarovaním bol hlavným zdrojom šumu detektora šum pochádzajúci z vyčítavacej elektroniky. Keď dávka v SiO₂ vrstve presiahne \approx 4 kGy, radiačné poškodenie spôsobí, že sa hlavným zdrojom šumu stane zvodový prúd. Hlavnou príčinou pozorovaného nárastu ofsetu a šumu bol teda nárast zvodového prúdu, ktorý zapríčinilo naindukované radiačné poškodenie.

Nárast šumu viedol aj k zhoršeniu energetického rozlíšenia detektora. V závislosti od dávky sa fotopík rozšíril približne o 115 eV/kGy.

Pre dávky nižšie ako 4 kGy sa zmena konverzného faktora neočakáva. Vzhľadom na distribúciu zväzku na ožarovanej ploche 20 pixelov \times 20 pixelov, jednotlivé pixely s vyššou absorbovanou dávkou vykazovali miernu zmenu konverzného faktora. Závislosť konverzného faktora od dávky je nízka, kvôli výraznej absorpcii žiarenia v objeme kremíkového senzora. Ak by sa však na ožarovanie použili fotóny s vyššou energiou, vyčítavacia elektronika by bola oveľa náchylnejšia na poškodenie. Napríklad, v prípade použitia 20 keV fotónov by bola absorbovaná dávka o tri rády vyššia, v porovnaní s 9 keV fotónmi.

Vzhľadom na absorbovanú dávku boli namerané zmeny v parametroch detektora použité na odhad životnosti tohto detektora. Životnosť detektora sa posudzovala vzhľadom na hodnoty parametrov, ktoré musí dosahovať pri experimentálnych meraniach. Výrazné zníženie dynamického rozsahu sa očakáva v prípade, že energia deponovaná v senzore počas jeho používania, presiahne dynamický rozsah ADC najmenej o päť rádov (pre $t_{\text{int}} = 800 \mu\text{s}$). Schopnosť rozlišovania jednotlivých 9 keV fotónov s rozlíšením $> 5 \sigma$ sa zachová, ak dávka nepresiahne 9 kGy pre $t_{\text{int}} = 800 \mu\text{s}$, a až do dávky 28 kGy pre $t_{\text{int}} = 50 \mu\text{s}$.

Uvedené experimentálne výsledky nie sú platné výhradne iba pre EuXFEL, ale sú aplikovateľné aj pre iné zariadenia. V blízkej budúcnosti plánujeme skúmať žiarenie senzora ako spôsob ozdravenia detektora a návrat k pôvodným parametrom. Ak by sa pozorovalo zhoršenie parametrov detektora, možnosť žiarenia by umožnila nápravu, bez nutnosti výmeny takto poškodeného detektora.

Prezentovaný výskum ukázal, že hlavný vplyv na zmenu parametrov mal nárast zvodového prúdu ako dôsledok radiačného poškodenia. Taktiež sa ukázalo, že čím je vyšší integračný čas, tým výraznejší je vplyv zvodového prúdu. Zobrazovacie detektory snímajúce s frekvenciou 4.5 MHz, majú integračný čas v rozmedzí desiatok až stoviek nanosekúnd. Napríklad integračný čas LPD detektora je $t_{\text{int}} = 90 \text{ ns}$. To je vyššie 500-násobné skrátenie času, v porovnaní so štandardným integračným časom ePix100a. Zvodový prúd LPD prispieva k celkovému šumu detektora 100-násobne menej v porovnaní s inými zdrojmi [13]. Inak povedané, aby bolo možné pozorovať nárast šumu spôsobený nárastom zvodového prúdu, integračný čas by musel byť o dva rády dlhší. Pri 4.5 MHz detektore teda platí, že jeho radiačné poškodenie nemôže byť vyhodnotených pomocou nárastu ofsetu alebo šumu. Vhodnejšími parametrami na sledovanie by v tomto prípade boli konverzný faktor alebo účinnosť zberu nosičov náboja. Pre efektívny zber náboja pri 4.5 MHz detektore je dôležitá pohyblivosť vytvoreného náboja, ktorá, ako bolo spomínané, sa radiačným poškodením znižuje.

Náš výskum ukázal, že radiačná odolnosť detektora ePix100a je dostatočná, pričom umožňuje niekoľkoročnú prevádzku bez výraznejšieho znehodnotenia jeho parametrov. Platí to za predpokladu, že energia deponovaná v pixeloch počas tohto obdobia nepresiahne 1 nJ. V takom prípade by primárnemu poškodeniu de-

tektora a jeho elektroniky dominovali iné mechanizmy, než procesy vyplývajúce z radiačného poškodenia.

References

1. TSCHENTSCHER, T. et al. Photon Beam Transport and Scientific Instruments at the European XFEL. *Applied Sciences*. 2017-06-09, vol. 7. Available from DOI: 10.3390/app7060592.
2. MARKOVIC, B. et al. Design and Characterization of the ePix100a: A Low Noise Integrating Pixel ASIC for LCLS Detectors. In: *2014 IEEE Nuclear Science Symposium and Medical Imaging Conference (NSS/MIC)*. 2014, pp. 1–3. Available from DOI: 10.1109/NSSMIC.2014.7431230.
3. HED. *Scientific Instrument HED* [online]. 2021 [visited on 2021-05-05]. Available from: https://www.xfel.eu/facility/instruments/hed/index_eng.html.
4. MADSEN, A. et al. Materials Imaging and Dynamics (MID) instrument at the European X-ray Free-Electron Laser Facility. *Journal of Synchrotron Radiation*. 2021-03, vol. 28, no. 2, pp. 637–649. Available from DOI: 10.1107/S1600577521001302.
5. GRAAFSMA, H. Requirements for and Development of 2 Dimensional X-ray Detectors for the European X-ray Free Electron Laser in Hamburg. *Journal of Instrumentation*. 2009-12-14, vol. 4, no. 12, pp. P12011.
6. KUSTER, Markus et al. Detectors and Calibration Concept for the European XFEL. *Synchrotron radiation news*. 2014-07-22, vol. 27, no. 4, pp. 35–38. Available from DOI: 10.1080/08940886.2014.930809.
7. ZHANG, Jianguo et al. Study of X-ray Radiation Damage in Silicon Sensors. *Journal of Instrumentation*. 2011-11, vol. 6, no. 11, pp. C11013–C11013. Available from DOI: 10.1088/1748-0221/6/11/c11013.
8. ZHANG, Jianguo et al. Investigation of X-ray Induced Radiation Damage at the Si-SiO₂ Interface of Silicon Sensors for the European XFEL. *Journal of instrumentation*. 2012-12, vol. 7, no. 12, pp. C12012. Available from DOI: 10.1088/1748-0221/7/12/c12012.
9. ZHANG, Jianguo et al. Study of X-ray Radiation Damage in the AGIPD Sensor for the European XFEL. *Journal of Instrumentation*. 2014, vol. 9, no. 05, pp. C05022. Available from DOI: 10.1088/1748-0221/9/05/C05022.

10. SCHWANDT, J et al. Optimization of the Radiation Hardness of Silicon Pixel Sensors for High X-ray Doses using TCAD Simulations. *Journal of Instrumentation*. 2012-01, vol. 7, no. 01, pp. C01006. Available from DOI: 10.1088/1748-0221/7/01/c01006.
11. SCHWANDT, Joern et al. Design and First Tests of a Radiation-Hard Pixel Sensor for the European X-Ray Free-Electron Laser. *IEEE Transactions on Nuclear Science*. 2014, vol. 61, no. 4, pp. 1894–1901. Available from DOI: 10.1109/TNS.2014.2304239.
12. KLANNER, R. et al. Challenges for Silicon Pixel Sensors at the European XFEL. *Nuclear Instruments and Methods in Physics Research Section A: Accelerators, Spectrometers, Detectors and Associated Equipment*. 2013, vol. 730, pp. 2–7. ISSN 0168-9002. Available from DOI: <https://doi.org/10.1016/j.nima.2013.05.166>.
13. KOCH, Andreas et al. Performance of an LPD Prototype Detector at MHz Frame Rates under Synchrotron and FEL Radiation. *Journal of Instrumentation*. 2013-11-04, vol. 8, no. 11, pp. C11001. Available from DOI: 10.1088/1748-0221/8/11/C11001.
14. JUNGSMANN-SMITH, JH et al. Radiation Hardness Assessment of the Charge-Integrating Hybrid Pixel Detector JUNGFRÄU 1.0 for Photon Science. *Review of Scientific Instruments*. 2015, vol. 86, no. 12, pp. 123110. Available from DOI: 10.1063/1.4938166.
15. ALLAHGHOLI, A et al. AGIPD, a High Dynamic Range Fast Detector for the European XFEL. *Journal of Instrumentation*. 2015-01-21, vol. 10, no. 01, pp. C01023. Available from DOI: 10.1088/1748-0221/10/01/C01023.
16. PORRO, Matteo et al. Development of the DEPFET Sensor with Signal Compression: A Large Format X-ray Imager with Mega-Frame Readout Capability for the European XFEL. *IEEE Transactions on Nuclear Science*. 2012-10-11, vol. 59, no. 6, pp. 3339–3351. Available from DOI: 10.1109/TNS.2012.2217755.
17. PORRO, Matteo et al. The MiniSDD-based 1-Megapixel Camera of the DSSC Project for the European XFEL. *IEEE Transactions on Nuclear Science*. 2021-04-29. Available from DOI: 10.1109/TNS.2021.3076602.
18. MARKOVIC, B et al. Design and Characterization of the ePix100a: A Low Noise Integrating Pixel ASIC for LCLS Detectors. In: *2014 IEEE Nuclear Science Symposium and Medical Imaging Conference (NSS/MIC)*. 2014-11-08, pp. 1–3. Available from DOI: 10.1109/NSSMIC.2014.7431230.

19. KLÁČKOVÁ, I et al. Characterization of the ePix100a and the FastCCD Semiconductor Detectors for the European XFEL. *Journal of Instrumentation*. 2019-01-07, vol. 14, no. 01, pp. C01008. Available from DOI: 10.1088/1748-0221/14/01/C01008.
20. DENES, P et al. A Fast, Direct X-ray Detection Charge-Coupled Device. *Review of Scientific Instruments*. 2009-08-06, vol. 80, no. 8, pp. 083302. Available from DOI: 10.1063/1.3187222.
21. JANUSCHEK, Friederike et al. Performance of the LBNL FastCCD for the European XFEL. In: *2016 IEEE Nuclear Science Symposium, Medical Imaging Conference and Room-Temperature Semiconductor Detector Workshop*. 2016-11-29, pp. 1–3. Available from DOI: 10.1109/NSSMIC.2016.8069829.
22. JUNGSMANN-SMITH, JH et al. JUNGFRÄU 0.2: Prototype Characterization of a Gain-Switching, High Dynamic Range Imaging System for Photon Science at SwissFEL and Synchrotrons. *Journal of Instrumentation*. 2014-12-15, vol. 9, no. 12, pp. P12013. Available from DOI: 10.1088/1748-0221/9/12/P12013.
23. HART, Mathew et al. Development of the LPD, a High Dynamic Range Pixel Detector for the European XFEL. In: *2012 IEEE Nuclear Science Symposium and Medical Imaging Conference Record (NSS/MIC)*. 2012-11-27, pp. 534–537. Available from DOI: 10.1109/NSSMIC.2012.6551165.
24. KUSTER, Markus et al. The 1-Megapixel pnCCD Detector for the Small Quantum Systems Instrument at the European XFEL: System and Operation Aspects. *Journal of Synchrotron Radiation*. 2021-03, vol. 28, no. 2, pp. 576–587. Available from DOI: 10.1107/S1600577520015659.
25. AFFOLDER, A et al. Silicon detectors for the sLHC. *Nuclear Instruments and Methods in Physics Research Section A: Accelerators, Spectrometers, Detectors and Associated Equipment*. 2011, vol. 658, no. 1, pp. 11–16. Available from DOI: 10.1016/j.nima.2011.04.045.
26. LINDSTRÖM, Gunnar. Radiation Damage in Silicon Detectors. *Nuclear Instruments and Methods in Physics Research Section A: Accelerators, Spectrometers, Detectors and Associated Equipment*. 2003-10-11, vol. 512, no. 1, pp. 30–43. ISSN 0168-9002. Available from DOI: 10.1016/S0168-9002(03)01874-6.
27. VAN LINT, Victor AJ et al. Mechanisms of Radiation Effects in Electronic Materials. Volume 1. *NASA STI/Recon Technical Report A*. 1980, vol. 81.
28. VAN GINNEKEN, A. *Nonionizing Energy Deposition in Silicon for Radiation Damage Studies*. 1989. Technical report. Fermi National Accelerator Laboratory.

29. MCLEAN, F Barry et al. *Basic Mechanisms of Radiation Effects in Electronic Materials and Devices*. 1987-09-01. Technical report. HARRY DIAMOND LABS ADELPHI MD.
30. MA, Tso-Ping et al. *Ionizing Radiation Effects in MOS Devices and Circuits*. John Wiley & Sons, 1989-04. ISBN 978-0-471-84893-6.
31. OLDHAM, Timothy R et al. Total Ionizing Dose Effects in MOS Oxides and Devices. *IEEE transactions on nuclear science*. 2003-07-09, vol. 50, no. 3, pp. 483–499. Available from DOI: 10.1109/TNS.2003.812927.
32. SZE, SM et al. *Semiconductor Devices: Physics and Technology, 3rd Edition*. Wiley Global Education, 2012-05. ISBN 978-0-470-53794-7.
33. CHANG, CP. Radiation Hardened N-Buried Channel CCD's Using Backside Phosphorus Gettering. *IEEE Transactions on Nuclear Science*. 1978-12, vol. 25, no. 6, pp. 1454–1458. Available from DOI: 10.1109/TNS.1978.4329552.
34. BLACKBURN, DL et al. The Effect of Ionizing Radiation on the Breakdown Voltage of Power MOSFETs. *IEEE Transactions on Nuclear Science*. 1983-12, vol. 30, no. 6, pp. 4116–4121. Available from DOI: 10.1109/TNS.1983.4333092.
35. PUGH, RD et al. Characteristics of the Breakdown Voltage of Power MOSFETs After Total Dose Irradiation. *IEEE Transactions on Nuclear Science*. 1986-12, vol. 33, no. 6, pp. 1460–1464. Available from DOI: 10.1109/TNS.1986.4334623.
36. SEXTON, Fred W et al. Correlation of Radiation Effects in Transistors and Integrated Circuits. *IEEE Transactions on Nuclear Science*. 1985-12, vol. 32, no. 6, pp. 3975–3981. Available from DOI: 10.1109/TNS.1985.4334053.
37. RANUAREZ, Juan C et al. A Review of Gate Tunneling Current in MOS Devices. *Microelectronics reliability*. 2006-12, vol. 46, no. 12, pp. 1939–1956. Available from DOI: 10.1016/j.microrel.2005.12.006.
38. NATHAN, V et al. Gate-Induced Drain Leakage Current in MOS Devices. *IEEE transactions on electron devices*. 1993-10, vol. 40, no. 10, pp. 1888–1890. Available from DOI: 10.1109/16.277353.
39. LARCHER, Luca et al. A Model of the Stress Induced Leakage Current in Gate Oxides. *IEEE Transactions on Electron Devices*. 2001-02, vol. 48, no. 2, pp. 285–288. Available from DOI: 10.1109/16.902728.
40. FANO, Ugo. Ionization Yield of Radiations. II. The Fluctuations of the Number of Ions. *Physical Review*. 1947-07, vol. 72, no. 1, pp. 26. Available from DOI: 10.1103/PhysRev.72.26.

41. LOWE, BG. Measurements of Fano factors in Silicon and Germanium in the Low-Energy X-ray Region. *Nuclear Instruments and Methods in Physics Research Section A: Accelerators, Spectrometers, Detectors and Associated Equipment*. 1997-11-11, vol. 399, no. 2-3, pp. 354–364. Available from DOI: 10.1016/S0168-9002(97)00965-0.
42. KNOLL, GF. *Radiation Detection and Measurement*. John Wiley & Sons, 2010-08. ISBN 978-0-470-13148-0.
43. BLAJ, G et al. X-ray Imaging with ePix100a: A High-Speed, High-Resolution, Low-Noise Camera. In: *Hard X-Ray, Gamma-Ray, and Neutron Detector Physics XVIII*. 2016-09-30, vol. 9968, 99680J. Available from DOI: 10.1117/12.2238136.
44. NISHIMURA, K et al. Design and Performance of the ePix Camera System. In: *AIP Conference Proceedings*. 2016-07-27, vol. 1741, p. 040047. No. 1. Available from DOI: 10.1063/1.4952919.
45. SOROKIN, Andrey A et al. An X-ray Gas Monitor for Free-Electron Lasers. *Journal of synchrotron radiation*. 2019-07, vol. 26, no. 4, pp. 1092–1100. Available from DOI: 10.1107/S1600577519005174.
46. MALTEZOPOULOS, Theophilos et al. Operation of X-ray gas monitors at the European XFEL. *Journal of Synchrotron Radiation*. 2019, vol. 26, no. 4. Available from DOI: 10.1107/S1600577519003795.
47. CANNY, John. A Computational Approach to Edge Detection. *IEEE Transactions on pattern analysis and machine intelligence*. 1986-11, no. 6, pp. 679–698. Available from DOI: 10.1109/TPAMI.1986.4767851.
48. LEI, F et al. MULASSIS: A Geant4-Based Multilayered Shielding Simulation Tool. *IEEE Transactions on Nuclear Science*. 2002, vol. 49, no. 6, pp. 2788–2793. Available from DOI: 10.1109/TNS.2002.805351.
49. PIA, MG et al. The Geant4 Toolkit: Simulation Capabilities and Application Results. *Nuclear Physics B-Proceedings Supplements*. 2003-09, vol. 125, pp. 60–68. Available from DOI: 10.1016/S0920-5632(03)90967-4.

List of Author's Publications

Scientific articles in peer reviewed (CC) journals

- [I] KLAČKOVÁ, I., et al. Characterization of the ePix100a and the FastCCD Semiconductor Detectors for the European XFEL. In *Journal of Instrumentation*. Vol. 14, (2019), Art. no. C01008 [11] s. (2019: 1.454 - IF, Q3 - JCR Best Q, 0.805 - SJR, Q1 - SJR Best Q)

Cited in:

ROVEZZI, Mauro, et al. TEXTS: In-Vacuum Tender X-ray Emission Spectrometer with 11 Johansson Crystal Analyzers. In *Journal of synchrotron radiation*, 2020, vol. 27, no., pp. 813-826. ISSN 0909-0495.

- [II] **Submitted and in review process** KLAČKOVÁ, I., et al. Radiation Hardness Study of the ePix100 Sensor and ASIC under Direct Illumination at the European XFEL. In *Journal of Instrumentation*.

Published scientific contributions at international conferences

- [III] JANUSCHEK, Friederike, KLAČKOVÁ, I., et al. Performance of the LBNL FastCCD for the European XFEL. In *2016 IEEE Nuclear Science Symposium, Medical Imaging Conference and Room-Temperature Semiconductor Detector Workshop*. IEEE, 2017, Art. no. 8069829 [3] s. ISBN 978-1-5090-1643-3.

Cited in:

MERCURIO, Giuseppe, et al. First Commissioning Results of the KB Mirrors at the SCS Instrument of the European XFEL. In *Advances in Metrology for X-Ray and EUV Optics VIII. International Society for Optics and Photonics*, 2019, vol. 11109, ISSN 0277-786X.

Published scientific contributions at domestic conferences

- [IV] KLAČKOVÁ, Ivana - ŠAGÁTOVÁ, Andrea - FÜLÖP, Marko - NEČAS, Vladimír. Homogeneity of Electron Accelerator Dose Distribution. In *APCOM 2015 : Proceedings of 21st international conference on applied physics of condensed matter. Štrbské Pleso, Slovak Republic. June 24-26, 2015*. vol. 1 Bratislava : STU, 2015, S. 248-251. ISBN 978-80-227-4373-0.